

Optical, structural, and chemical properties of flash evaporated In_2S_3 buffer layer for $\text{Cu}(\text{In,Ga})\text{Se}_2$ solar cells

Rajneesh Verma,^{1,a)} Debjit Datta,² Adrian Chirila,¹ Dominik Güttler,¹ Julian Perrenoud,¹ Fabian Pianezzi,¹ Ulrich Müller,³ Satyendra Kumar,² and Ayodhya N. Tiwari¹

¹Laboratory for Thin Films and Photovoltaics, EMPA, Überlandstrasse 129, CH-8600 Dübendorf, Switzerland

²Department of Physics and Samtel Centre for Display Technologies (SCDT), Indian Institute of Technology Kanpur, Kanpur 208016, India

³Laboratory for Nanoscale Materials Science, EMPA, Überlandstrasse 129, CH-8600 Dübendorf, Switzerland

(Received 29 April 2010; accepted 20 August 2010; published online 8 October 2010)

In_2S_3 layers were deposited by flash evaporation technique with varying flash rates. The optical constants of layers based on Tauc–Lorentz model dielectric function were extracted from spectroscopic ellipsometry measurements. X-ray photoelectron spectroscopic investigation revealed the presence of oxygen impurity in as-deposited and air-annealed layers with traces of Na inclusion in the layer grown at high flash rate. The enhancement in crystalline arrangement of as-deposited layer after air annealing was confirmed by Raman spectroscopy. Rutherford backscattering measurements revealed the growth of off-stoichiometric layers at all flash rates. An analytical layer growth model has been proposed supporting the results obtained by various layer characterization techniques. The solar cells were prepared with flash evaporated In_2S_3 buffer layers and their performances were compared with CdS reference solar cell. A significant gain in short-circuit current was obtained after air annealing of the complete device at 200 °C for 20 min. A maximum conversion efficiency of 12.6% was delivered by a high flash rate In_2S_3 buffered cell with open-circuit voltage close to that of CdS reference cell. The improvement in device performance after air annealing treatment is explained by thermally enhanced Cu and oxygen diffusion from $\text{Cu}(\text{In,Ga})\text{Se}_2$ and *i*-ZnO to In_2S_3 layer, respectively. © 2010 American Institute of Physics. [doi:10.1063/1.3490624]

I. INTRODUCTION

The optoelectronic properties of III–VI semiconductor In_2S_3 makes it a material of choice in optoelectronic and photovoltaic (PV) applications.^{1,2} The interest in using In_2S_3 and its derivative compounds as buffer layer in $\text{Cu}(\text{In,Ga})\text{Se}_2$ (CIGS) thin film solar cell technology stems from the fact that they serve as a better replacement to conventional CdS buffer layer deposited by chemical bath deposition method.^{3,4} The electrical, optical, structural, and morphological properties of In_2S_3 layer have been found to be a strong function of its method of preparation.^{5–16} The single crystal In_2S_3 has a direct band gap (E_g) of 1.98 eV,⁵ whereas the band gap (direct or indirect) of thin film In_2S_3 may vary from 2.0 to 2.9 eV depending upon its deposition technique and doping concentration.^{6–16} Among wide range of thin film deposition techniques, the physical vapor deposition (PVD) technique has immense potential to meet the requirements for industrial production of large area solar cells and modules. The solar cell efficiency comparable to that of standard CdS reference cells has been achieved with PVD- In_2S_3 buffered CIGS solar cell.^{4,17,18} It is known that the thermal evaporation of In_2S_3 material results in growth of a nonstoichiometric layer with respect to sulfur content.¹⁷ The compositional deviation from stoichiometric In_2S_3 in the buffer

layer may limit the solar cell performance. We have attempted to address the issue of nonstoichiometry in the evaporated In_2S_3 layer by exploiting flash evaporation technique which has potential to form film with stoichiometric composition.¹⁹ Additionally, flash evaporation is an industrially significant and highly desired technique due to:

- (i) Fast deposition: deposition time can significantly be reduced in comparison to conventional thermal evaporation technique.
- (ii) High process yield: amount of source material, which largely depends on the desired thickness of layer, to be evaporated can easily be optimized.
- (iii) Easily up-scalable: easy modification and implementation to large area deposition system with continuous feed-in of the source materials.
- (iv) Control over film composition.
- (v) In-line deposition compatibility: adaptive to vacuum based deposition sequences in solar cell fabrication on continuously moving substrate such as polymer foils.

In this work, we present a detailed ellipsometric study on In_2S_3 layers deposited at varying flash rates. The ellipsometric modeling performed with emphasis on the choice of multilayer stack model and model dielectric function yielded optical constants and associated optical parameters of the layers. The optical characterization led to an in-depth understanding of structural and chemical properties of flash- In_2S_3

^{a)}Electronic mail: rajneesh.verma@empa.ch.

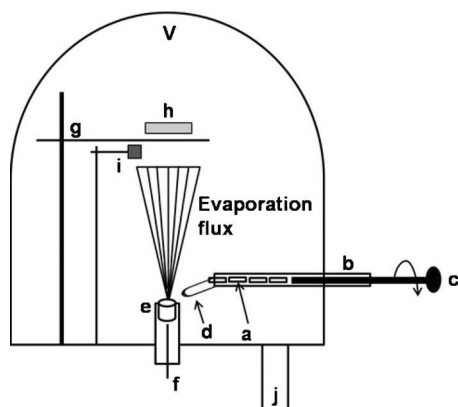


FIG. 1. Schematic diagram (not to scale) of an in-house developed vacuum chamber (V) for flash evaporation: (a) In_2S_3 pellet, (b) pellet injector, (c) roller, (d) pellet guide, (e) evaporation crucible, (f) thermocouple, (g) substrate shutter, (h) substrate, (i) quartz crystal, and (j) vacuum pump.

layers. The PV characteristics of the solar cells with In_2S_3 buffer layer deposited at varying flash rates were analyzed and compared with CdS reference solar cell.

II. EXPERIMENTAL

A. Flash evaporation

The flash evaporation of In_2S_3 source material was carried out in an *in-house* developed vacuum deposition system. Figure 1 shows the schematic diagram of the vacuum deposition chamber (V) describing its various components (a–j). The pellets of In_2S_3 material (a) are loaded in pellet injector (b). The roller (c) attached to pellet injector pushes the pellets toward the pellet guide (d). The pellet in contact with pellet guide is then directed toward the source evaporation crucible (e) kept at an elevated temperature as measured by a thermocouple (f). This results in sudden generation of an evaporation flux, “flash”, of In_2S_3 source material. On opening the substrate shutter (g), the flux constituents condense on the substrate (h) forming a thin layer of the evaporated material. The thickness of the deposited layer is monitored by quartz crystal monitor (i). The In_2S_3 layer of ~ 50 nm thickness was deposited on different substrates at three different flash rates, corresponding to three different evaporation crucible temperatures (T_{crucible}), labeled as low ($T_{\text{crucible}} = 950^\circ\text{C}$), moderate ($T_{\text{crucible}} = 1050^\circ\text{C}$) and high ($T_{\text{crucible}} = 1150^\circ\text{C}$) flash rate.

B. In_2S_3 film characterization

The optical properties of In_2S_3 layers, as-deposited and annealed in air for 10 min at 200°C (referred as air-annealed, henceforth), were investigated by spectroscopic ellipsometry technique. The ellipsometric measurements were performed using a phase modulated spectroscopic ellipsometer (UVISSEL, Horiba Jobin Yvon) at a fixed incident angle of 70° in a wide spectral range of 280–1650 nm. X-ray photoelectron spectra were measured on a Physical Electronics Quantum 2000 system using monochromated $\text{Al } K_\alpha$ ($h\nu = 1486.6$ eV) radiation. The electron takeoff angle was 45° and the analyzer was operated in the constant pass energy mode. The beam diameter was typically $100\ \mu\text{m}$. Sputtering

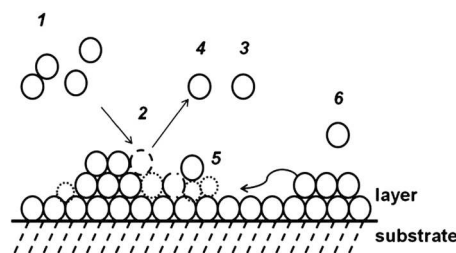


FIG. 2. Schematic two-dimensional illustration of growth model of flash evaporated In_2S_3 layer: (1) impinging adatoms, (2) atomic displacement, (3) reflection, (4) knock-out, (5) densification, (6) re-evaporation, and lattice damage (dotted circles).

was done with Ar-ions at an acceleration energy of 1 kV for 20 s corresponding to the removal of a ~ 0.6 nm thick layer on Ta_2O_5 . Quantitative analysis was done with the PHI MultiPak V8.2b software package from the manufacturer. The Rutherford backscattering (RBS) measurements (2 MeV, He^+ ions) were performed to determine the chemical composition of the layers. The roughness and morphology of the layers were investigated by atomic force microscopy (AFM) in tapping mode. The Raman scattering measurements were performed in the range of $70\text{--}470\ \text{cm}^{-1}$ using He–Ne laser ($\lambda = 633\ \text{nm}$).

C. CIGS solar cells

CIGS layer was grown on Mo coated soda-lime-glass (SLG) substrate kept at 550°C by coevaporation of constituent elements using a modified three-stage process described elsewhere.²⁰ The In_2S_3 buffer layer of ~ 50 nm thickness was then deposited followed by the deposition of a window bilayer of ZnO:Al/ZnO by rf-sputtering. The solar cell was completed by depositing Ni/Al metal contact grid resulting in layer stack structure represented by SLG/Mo/CIGS/buffer/ ZnO/ZnO:Al/Ni-Al . No antireflection coating was applied to any of the cells in the present work. The current density-voltage (J - V) characteristic of the solar cell was measured under simulated AM 1.5G illumination (25°C , $1000\ \text{W/m}^2$) condition and the internal quantum efficiency (IQE) was determined to investigate the collection losses of photogenerated carriers.

III. RESULTS AND DISCUSSION

A. Layer growth model

The growth mechanism of the flash evaporated layer can be understood with the help of an analytical model illustrated in Fig. 2. Owing to the inherent nature of flash evaporation technique, the adatoms (1) of the source material, comprising of evaporation flux (flash), arrive at the substrate surface with high kinetic energy. The high kinetic energy renders high surface mobility to adatoms resulting in enhanced surface diffusion (curved arrow) necessary for growth of a continuous layer. On encountering a nucleation center, the nuclei grow and form monolayer.

The monolayer subsequently formed is bombarded with a continuous flux of energetic adatoms which may give rise to secondary effects namely, atom displacement (2), reflection (3), knock-out (4), lattice damage (dotted circle), strain

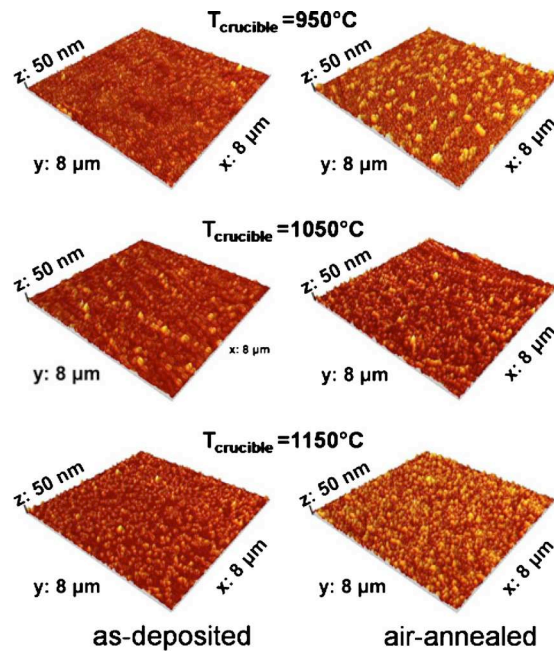


FIG. 3. (Color online) AFM micrographs of as-deposited and air-annealed In_2S_3 layers grown on SLG substrate at different flash rates.

etc. The incessant collision between arriving adatoms and already grown monolayer may impart compactness (5) to the layer at the cost of secondary events. During growth, the energy of impinging adatoms is dissipated to already grown monolayer which may lead to a reverse evaporation of adatoms (6). Hence, layers are expected to grow denser with chemical and structural imperfections that may further enhance with rise in flash rate. The growth characteristic of flash evaporated buffer layer deposited on SLG substrate at room temperature was studied by AFM technique. The AFM micrographs shown in Fig. 3 revealed the continuous growth of In_2S_3 layer with granular morphology. The grain growth due to air annealing led to a distinct morphological contrast among layers. The root-mean-square roughness was estimated to be 2–3 nm.

B. Spectroscopic ellipsometry

Spectroscopic ellipsometry is a powerful tool for characterization of thin films. A wealth of information such as, optical constants, thickness, growth characteristics, and crystallinity of thin films can be obtained with high degree of precision.²¹ Not only the band gap of the buffer layer is important for ensuring higher short-circuit current (J_{sc}) in blue wavelength region of solar spectrum, but also the optical reflection losses from the solar cell need to be minimized.²² Hence, the combination of higher band gap and appropriate match among refractive indices of various layers present in the solar cell can give rise to higher conversion efficiency.

Pervious optical studies on In_2S_3 layers were primarily focused on determination of type of optical transitions, energy band gap, and optical constants using transmission and reflection measurements.^{8,14,23,24} Due to negligence or (and) improper consideration of the light scattering effects originating from surface roughness, grain boundaries, film thick-

ness, and compositional nonuniformity, the results obtained from transmission and reflection measurements can readily be misinterpreted. The success of ellipsometric analysis largely depends on selection of a suitable multilayer stack model (representing the surface roughness and various interfaces) and a model dielectric function. Although there are (scarce) reports on ellipsometric investigations of In_2S_3 layers,^{25,26} a thorough analysis describing the suitable multilayer stack model and model dielectric function to extract accurate optical constants is lacking in the literature.

1. Model description

a. Ellipsometric model fitting. The model fitting for ellipsometric analysis was performed using Marquardt–Levenberg fitting technique for minimization of the mean square error given by

$$\chi^2 = \left[\frac{1}{2M - P} \right] \sum_{i=1}^M \{ [I_s^{\text{exp}}(\lambda) - I_s^{\text{cal}}(\lambda)]^2 + [I_c^{\text{exp}}(\lambda) - I_c^{\text{cal}}(\lambda)]^2 \}, \quad (1)$$

where M and P are the total number of experimental data points and model parameters, respectively. The fitting raw data $[I_s(\lambda)$ and $I_c(\lambda)]$ determine the signal detected by the ellipsometer given by

$$I(\lambda) = I_0(\lambda) + I_s(\lambda) \sin \delta(t) + I_c(\lambda) \cos \delta(t), \quad (2)$$

where $\delta(t)$ is the induced phase shift by modulator in the ellipsometric setup and $I_0(\lambda)$ is a function of the ellipsometric angles and the angles of the polarizer, analyzer, and the modulator from the plane of incidence. In our experimental setup, the polarizer, analyzer, and the modulator angles were configured to set $I_0(\lambda) \sim 1.0$.

b. Multilayer stack model. To account for surface roughness and In_2S_3 /SLG interface, we used a trilayer stack model, wherein the bottom layer (optically infinite), middle layer, and the top layer represent the SLG substrate, In_2S_3 thin film, and the In_2S_3 film roughness, respectively. Bruggeman effective medium approximation was used for the top layer comprising of dielectric functions of In_2S_3 and void ($n \sim 1$, $k \sim 0$). Thicknesses of the middle layer and the top layer were initially estimated by multiple pretrials in nonabsorbing optical range of the In_2S_3 film (800–1650 nm). For final thickness values presented here, the thickness parameters were estimated along with other fitting parameters of the model dielectric function.

c. Model dielectric function. Earlier reports on ellipsometric studies of In_2S_3 thin films either extracted the optical constants using direct inversion of the ellipsometric raw data or incorporated classical-oscillator (CO) and Forouhi–Bloomer (FB) model dielectric functions to extract the optical parameters and the optical constants.^{23,26} However, the recent ellipsometric investigations on various thin films indicate that the choice of proper model dielectric function, in terms of the Kramer–Kronig consistency and the presence of optical band gap as a model parameter, is crucial for extraction of reliable optical parameters and the resultant optical constants.^{27–30} A detailed description of the commonly used model dielectric functions such as CO model, FB model, and

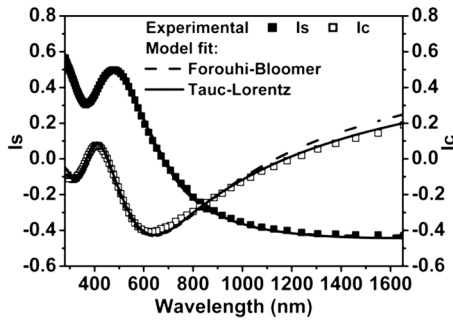


FIG. 4. Ellipsometric best fit for In_2S_3 layers using FB and TL model dielectric functions and a trilayer stack model.

Tauc-Lorentz (TL) model for the analysis of thin films and their limitations can be found elsewhere.^{27,30} The extinction coefficient (k) and index of refraction (n) derived from FB model are given by Eqs. (3) and (4), respectively,

$$k(E) = \sum_{n=1}^N \frac{A_{n\text{FB}}(E - E_{g\text{FB}})^2}{E^2 - B_{n\text{FB}}E + C_{n\text{FB}}}, \quad (3)$$

$$n(E) = \sqrt{\varepsilon_{\infty\text{FB}}} + \sum_{n=1}^N \frac{B_{0n\text{FB}}E + C_{0n\text{FB}}}{E^2 - B_{n\text{FB}}E + C_{n\text{FB}}}, \quad (4)$$

where N is the total number of optical transitions, $A_{n\text{FB}}$, $B_{n\text{FB}}$, and $C_{n\text{FB}}$ are fitting parameters for n th optical transition, $E_{g\text{FB}}$ is the energy band gap, $B_{0n\text{FB}}$ and $C_{0n\text{FB}}$ are functions of $A_{n\text{FB}}$, $B_{n\text{FB}}$, $C_{n\text{FB}}$, and $E_{g\text{FB}}$, and $\varepsilon_{\infty\text{FB}}$ is the high frequency dielectric constant. The TL model, consistent with Kramer-Kronig relation, is based on the consideration of Tauc's density of states above band edge and Lorentz oscillator model for oscillating electron in the optical electric field.²⁹ The imaginary part of the complex dielectric function [$\varepsilon(E) = \varepsilon_r(E) + i\varepsilon_i(E)$] is given by

$$\varepsilon_i(E) = \frac{1}{E} \times \frac{A_{\text{TL}} \times E_{0\text{TL}} \times C_{\text{TL}} \times (E - E_{g\text{TL}})^2}{(E^2 - E_{0\text{TL}}^2)^2 + C_{\text{TL}}^2 \times E^2}, \quad (5)$$

where, A_{TL} , $E_{0\text{TL}}$, C_{TL} , and $E_{g\text{TL}}$ are the amplitude, peak transition energy, broadening and the optical band gap, respectively. The real part of the dielectric function is calculated by Kramers-Kronig integration of the imaginary part and is given by

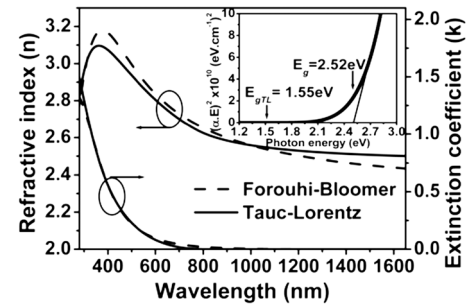


FIG. 5. Optical constants of In_2S_3 layer obtained from FB and TL model fitting. Inset shows the method of band gap extraction from absorbance spectrum.

$$\varepsilon_r(E) = \varepsilon_{\infty\text{TL}} + \frac{2}{\pi} P \cdot \int_{E_{g\text{TL}}}^{\infty} \frac{\xi \cdot \varepsilon_i(\xi)}{\xi^2 - E^2} \cdot d\xi, \quad (6)$$

where P indicates the principle value of the integration performed for energies above the band gap and $\varepsilon_{\infty\text{TL}}$ is the high frequency dielectric constant. Figure 4 presents FB and TL model fitting of ellipsometric raw data obtained from flash- In_2S_3 layer grown on SLG substrate. Figure 5 shows the corresponding refractive index and extinction coefficient of the In_2S_3 layer. The inset in Fig. 5 demonstrates the general approach of extracting optical band gap from Tauc's plot by linear extrapolation of $(\alpha E)^2$ to the energy axis. Clearly, there exists nonzero absorption at energies below the band gap (E_g). A model dielectric function, incorporating band gap as a fitting parameter can be used to extract the absorption edge directly from the ellipsometric analysis. This is based on the consideration of parabolic density of states near the band edge and can be represented by $E_{g\text{MODEL}}$. However, the $E_{g\text{MODEL}}$ has been often found to be dependent on the model dielectric function used for the analysis.

Table I presents the optical parameters extracted using FB and TL models for as-deposited and air-annealed In_2S_3 layers. The band edge extracted using FB model ($E_{g\text{FB}} = 0.97$ eV) was found to be lower than that extracted using the TL ($E_{g\text{TL}} = 1.55$ eV) model. This is consistent with our previous ellipsometric investigations, wherein the extracted band gap from FB model was consistently lower than the band gap extracted from the TL model.²⁷ As shown in Fig. 5, fitting from FB model led to nonzero extinction coefficient below wavelength ~ 990 nm. Since, FB model leads to sub-band absorption ($\alpha > 0$ for $E < E_{g\text{FB}}$), it is fundamentally in-

TABLE I. Optical parameters of flash- In_2S_3 layers (as-deposited and air-annealed) extracted from spectroscopic ellipsometry using FB and TL model dielectric functions and a trilayer stack model.

T_{crucible} (°C)	Layer	FB				TL			
		A_{FB}	B_{FB} (eV)	C_{FB} (eV) ²	$E_{g\text{FB}}$ (eV)	A_{TL} (eV)	$E_{0\text{TL}}$ (eV)	C_{TL} (eV)	$E_{g\text{TL}}$ (eV)
950	As-deposited	0.47 ± 0.04	7.2 ± 0.01	16.6 ± 0.5	0.97 ± 0.08	75.7 ± 2.8	4.78 ± 0.03	3.9 ± 0.1	1.55 ± 0.02
	Air-annealed	0.34 ± 0.03	8.7 ± 0.1	22.6 ± 0.7	0.9 ± 0.1	89.1 ± 3.0	5.17 ± 0.02	4.11 ± 0.12	1.91 ± 0.03
1050	As-deposited	0.45 ± 0.03	0.75 ± 0.01	16.8 ± 0.5	1.13 ± 0.08	139 ± 10.9	4.3 ± 0.07	4.9 ± 0.3	1.95 ± 0.03
	Air-annealed	0.38 ± 0.03	7.7 ± 0.1	17.0 ± 0.6	1.51 ± 0.08	117.4 ± 3.9	4.6 ± 0.05	4.4 ± 0.1	2.04 ± 0.02
1250	As-deposited	0.46 ± 0.04	7.4 ± 0.1	16.7 ± 0.6	1.03 ± 0.08	135.2 ± 9.8	4.33 ± 0.06	4.66 ± 0.28	1.88 ± 0.03
	Air-annealed	0.43 ± 0.03	7.5 ± 0.1	16.6 ± 0.6	1.47 ± 0.08	117.4 ± 4.5	4.75 ± 0.06	4.4 ± 0.14	1.99 ± 0.03

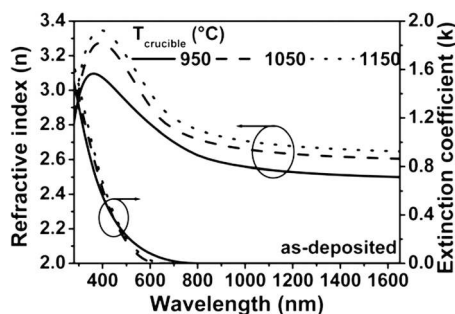


FIG. 6. Optical constants of as-deposited In_2S_3 layers grown at different flash rates.

consistent for Kramer–Kronig relation derived from principle of Causality. Whereas, in case of TL model, the subband gap absorption is strictly restricted by $\alpha=0$ for $E < E_{\text{gTL}}$. Notably, the E_{gTL} is lower than the band gap (E_{g}) extracted from the absorption spectra. For energies between the E_{gTL} and E_{g} ($E_{\text{gTL}} < E < E_{\text{g}}$), the absorption is often exponential due to the disordered amorphous nature of the film.³¹ From the model fitting, the Penn gap was extracted to be between 4.3 and 4.8 eV for layers grown at varying flash rates. It can be inferred from Fig. 4 that an excellent fit was obtained by TL model in the entire optical range. The similar results on the suitability of TL model have been reported by Datta *et al.*^{27,30} Based on above discussion, the TL model was used to determine the optical constants of In_2S_3 layers in this study.

2. Optical properties

The optical constants of as-deposited and air-annealed In_2S_3 layers grown with varying flash rates were extracted using TL model and are shown in Figs. 6 and 7, respectively. In case of as-deposited layers, an increase in refractive index with rise in flash rate indicated the densification and presence of different structural arrangements, inherent to growth mechanism described in Sec. III A, in the layers (Fig. 6). The drop in flash rate dependent refractive index accompanied by the blue shift in extinction coefficient was determined in air-annealed layers (Fig. 7). The similar values of band gap energy (2.5–2.55 eV) were calculated for layers deposited at three different flash rates (inset Fig. 7). The band gap increased to 2.8 eV, 2.73 eV, and 2.61 eV after air annealing treatment of layers grown at low, moderate, and high flash

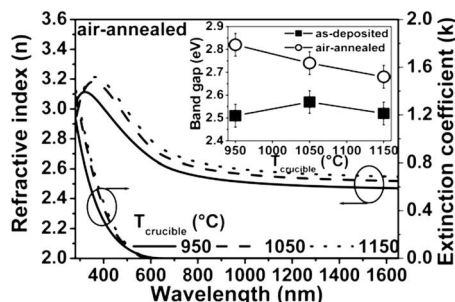


FIG. 7. Optical constants of air-annealed In_2S_3 layer grown at different flash rates. The inset shows the variation in energy band gaps of layer before and after air annealing (line connecting the data points in inset serves as an eye-guide).

rate, respectively. The x-ray photoelectron spectroscopic (XPS) measurements revealed the presence oxygen impurity in In_2S_3 layer. In addition, a trace amount of Na impurity was also detected in layer grown at high flash rate, which further increased after air annealing treatment. The concentration of oxygen impurity in the layer was found to be proportional to flash rate and increased after air annealing of the layer. The oxygen incorporation in In_2S_3 as $\text{In}_2\text{S}_{3-3x}\text{O}_{3x}$ has been identified to cause lattice compression giving rise to band gap widening.^{32,33} Additionally, Na incorporation in In_2S_3 also induces band gap widening and it tends to occupy tetrahedral vacant In (V_{In}) sites.^{34,35} Interestingly, contrary to anticipated increase in band gap with amount of oxygen inclusion (proportional to flash rate), the band gap showed weak dependence and inverse relationship with flash rate for as-deposited and air-annealed layers, respectively. The band gap of thin film semiconductor may strongly be affected by the imperfections such as grain size, grain boundaries, orientation, nonstoichiometry, defect level, localized charges, strain, and crystallinity present in the film. Quantum mechanical considerations suggest the generation of localized midband gap states due to structural and thermal disorder present in the film,^{31,36} consequently, decreasing the band gap.

The photoluminescence (PL) characterization of In_2S_3 layer indicated the presence of intermediate defect states generated due to chemical disorder present in the layer.³⁷ An experimental evidence of existence of intermediate defect states related to point defects of In (In_i) interstitial and occupancy of sulfur vacancy by oxygen (O_{Vs}) was obtained from room temperature PL measurements (not shown here) of flash- In_2S_3 layers. Therefore, the existence of localized defect states in the band gap can be visualized as a consequence of growth of structurally (Sec. III C) and chemically (Sec. III D) disordered layer deposited by flash evaporation technique (layer growth model in Sec. III A). These defect states originated from structural and chemical disorder in the layer may negate the effect of oxygen and Na incorporation into In_2S_3 thin film on band gap widening (inset Fig. 7) resulting in similar values of E_{g} .

AFM morphological study of the layer (Fig. 3) indicated the grain growth and recrystallization in the layer after air annealing treatment. The thermally driven structural rearrangements in the layer may result in lowering of disorder in the layer and thus, increasing the band gap energy (inset Fig. 7) as a consequence of annihilation of intermediate defect states. In addition to blue shift in extinction coefficient (increment in band gap) after air annealing, it also decreased indicating weaker photon absorption by electron transition due to thermally assisted annihilation of intermediate defect states.

The XPS analysis, described in Sec. III D, confirmed a significant increase in oxygen concentration in the layer as a result of air annealing. The layer grown at low flash rate (less structurally defective) showed the largest increase in band gap compared to layers grown at moderate and high flash rate which possessed higher defect density and hence, have lesser effect of oxygen inclusion on band gap widening caused by air annealing. Moreover, the structural modifications owing to air annealing may favor the relaxation process

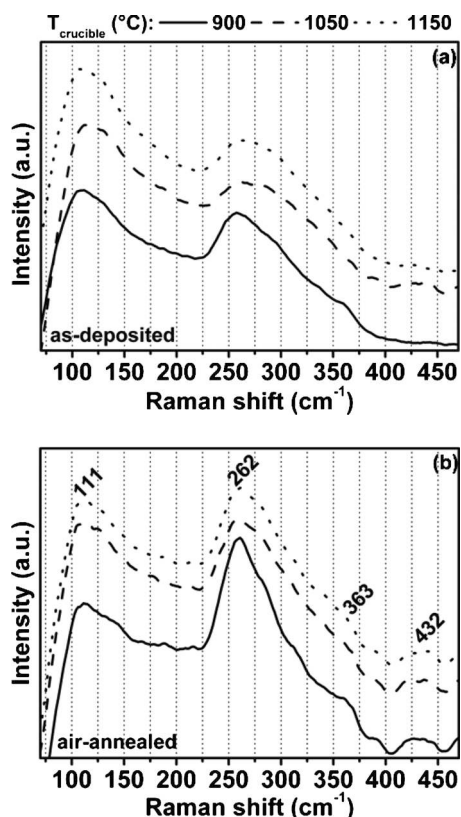


FIG. 8. Raman spectra of as-deposited (a) and air-annealed (b) In_2S_3 layer grown at low flash rate.

in highly disordered layer causing decrease in layer density which is implied by decrease in refractive index after air annealing treatment (Fig. 7). It should be pointed out that in case of layers grown at moderate and high flash rate, the air annealing temperature of 200 °C is not high enough to annihilate the same order of defects as it does in case of low flash rate layer. Therefore, higher annealing temperature is required for moderate and high flash rate layers to obtain the same increment in the band gap as observed in layer deposited at low flash rate.

C. Structural investigation

As discussed above, different refractive indices of as-deposited and air-annealed layers suggest structural disparities in the layers as a result of flash evaporation (Secs. III A and III B 2). The structural information of the flash- In_2S_3 layers was extracted by recording their Raman spectra shown in Fig. 8. The Raman signals corresponding to $\beta\text{-In}_2\text{S}_3$ phase was detected in as-deposited [Fig. 8(a)] and air-annealed layers [Fig. 8(b)]. Notably, the peak shift in as-deposited layer grown at three different flash rates was observed, which can be attributed to lattice perturbation caused by oxygen or/and sodium inclusion in crystalline $\beta\text{-In}_2\text{S}_3$ matrix. Furthermore, the peak broadening with rise in flash rate further suggested the lowering of crystalline arrangement (increase in structural imperfection) in the moderate and high flash rate layers. The air annealing of the layers resulted in enhanced crystalline character of the layers as evident from Fig. 8(b).

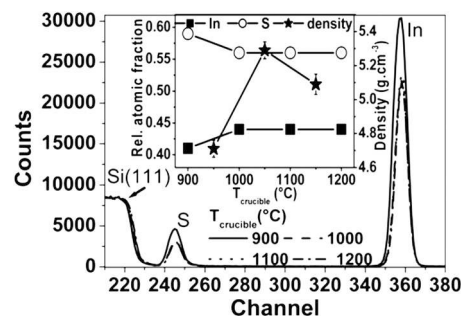


FIG. 9. RBS spectra of In_2S_3 layers deposited at different flash rates. The inset shows the atomic fraction and the density of layers evaluated from RBS measurement (line connecting the data points in inset serves as an eye-guide).

D. Chemical composition

The RBS measurements were performed to determine the chemical composition of layers grown on Si substrate at three different flash rates in the same deposition run. Contrary to expected stoichiometric growth of the deposit by flash evaporation technique, a substantial shift in chemical composition from stoichiometric In_2S_3 was measured. Figure 9 shows the RBS spectra of layers with inset showing the layer density and relative concentration (atomic fraction) of elements (In and S) detected in the layers. As indicated in the figure, the layers were found to be sulfur deficient with overall chemical composition given by In_2S_x , where $2.47 \leq x \leq 2.8$. It should be emphasized that compositional shift broadened (x decreased) with rise in flash rate indicating higher the flash rate, higher is sulfur-loss in the layer.

Miller and Searcy^{38,39} reported the dissociation of $\text{In}_2\text{S}_3(\text{s})$ in $\text{In}_2\text{S}(\text{g})$ and $\text{S}_2(\text{g})$ constituents and identified the occurrence of congruent dissociation in slightly sulfur-poor indium sulfide material. The higher evaporation temperature and large difference in the partial pressure of dissociated constituents [$p(\text{In}_2\text{S}) \sim 10^3 p(\text{S}_2)$, in the present case] may assist the growth of a nonstoichiometric layer as a consequence of incongruent dissociation of the source material.^{39–41} This suggests that the flash evaporation of In_2S_3 with present evaporation parameters (pallet composition and evaporation crucible temperature ≥ 950 °C) may favor incongruent dissociation of In_2S_3 material causing a significant deviation from stoichiometric In_2S_3 composition in the deposited layer. It can be speculated that the degree of incongruent dissociation may enhance with increase in flash rate (evaporation temperature). Additionally, the re-evaporation of sulfur from layer may further add to nonstoichiometry in the layer. This explains the higher sulfur deficiency in the layer grown at high ($\text{In}_2\text{S}_{2.47}$) and moderate ($\text{In}_2\text{S}_{2.55}$) flash rate than that in low ($\text{In}_2\text{S}_{2.8}$) flash rate layer. As evident from RBS investigations, although nonstoichiometric but stable chemical composition of the layer was attainable at higher flash rates ($T_{\text{crucible}} > 1050$ °C) deposition condition (inset of Fig. 9). Additionally, it should also be noticed from the RBS spectra that the layer deposited with lower ($T_{\text{crucible}} = 900$ °C) flash rate was thicker than one deposited at higher flash rates in which reflection and re-evaporation events illustrated in Fig. 2 are likely to play a

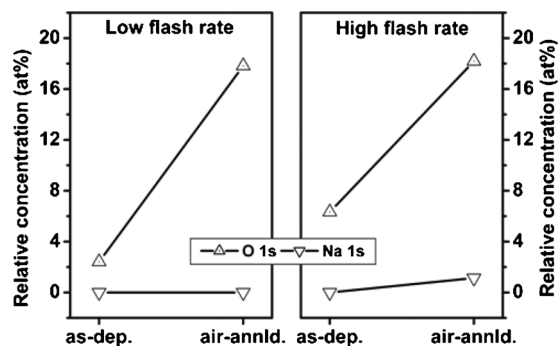


FIG. 10. Relative concentration of oxygen and sodium impurities deduced from XPS measurements on as-deposited and air-annealed In_2S_3 layer grown at low and high flash rates (line connecting the data points serves as an eye-guide).

significant role. The layer thickness measured by profilometer was used to determine the layer density from RBS analysis. With strong dependence on flash rate, the layer density increased with rise in flash rate (inset of Fig. 9). Notably, a small decrease in density of high flash rate layer, compared to layer grown at moderate flash rate, can be attributed to inhomogeneity in packing density of the adatoms in layer grown at high flash rate. A relative $\sim 7\%$ decrease in film density was calculated after air annealing indicating the occurrence of thermally driven restructuring or relaxation processes in the layers. The layer density considerations are in agreement with variation in refractive index before and after air annealing discussed in Sec. III B 2.

The XPS investigation revealed the oxygen and sodium impurity inclusion into the layers. The relative oxygen and sodium concentrations extracted from XPS measurements on layers grown at low and high flash rates are plotted in Fig. 10. The as-deposited layers were found to be contaminated with oxygen impurity. The oxygen concentration increased with increase in flash rate combined with a further increment after air annealing treatment. Furthermore, a trace amount of Na impurity in as-deposited high flash rate layer was also detected which further increased with subsequent air annealing step. These observations implied high concentration of defect centers present in the layer grown at high flash rate than that existing in low flash rate layer. It is well documented that the cationic impurity such as Cu^+ and Na^+ cannot only fill vacant tetrahedral In sites (V_{In}) but also substitute In atom in In_2S_3 matrix.^{34,42,43} Under the influence of a net concentration gradient, arising from large defect density in buffer layer, across buffer/SLG system, Na may diffuse from SLG substrate into buffer layer even at room temperature. Consequently, Na may not only fill vacant In sites but also it can replace In in In_2S_3 matrix. In addition, compared to as-deposited low flash rate layer, the higher oxygen and sodium content in high flash rate layer suggested that the layer grown at high flash rate possessed larger concentration of chemically active defects.

The XPS analysis compiles well with the RBS investigation emphasizing that high flash rate leads to higher degree of chemical disorder in the layer and as a result, the layer grown at high flash rate is likely to be more contaminated than one grown at low flash rate. Hence, based on the dis-

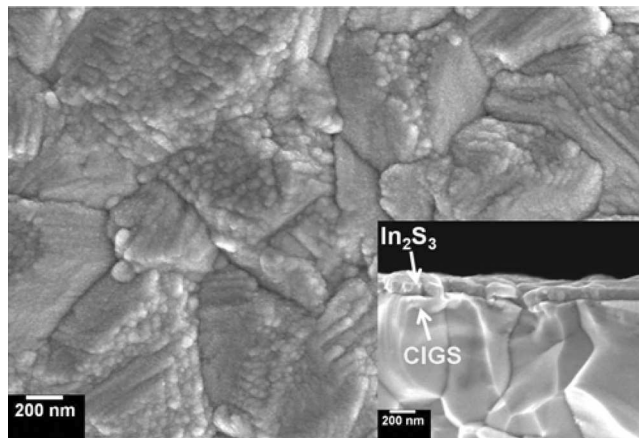


FIG. 11. SEM plan-view and cross-section micrographs of In_2S_3 /CIGS layer stack.

cussion in Secs. III B 2, III C, and III D it can be outlined that higher the flash rate, higher is the degree of structural and chemical disorder present in the layer.

E. CIGS solar cell buffered with flash- In_2S_3 layer

In_2S_3 layers were deposited on CIGS/Mo/SLG substrate ($T_{\text{substrate}}$ = room temperature) at three different flash rates. Figure 11 shows the scanning electron micrographs of the In_2S_3 layer deposited at low flash rate on CIGS surface. Although In_2S_3 layers conformally covered the rough CIGS surface, infrequent discontinuity at the large CIGS grain edges was distinguishable, indicating poor adhesion between CIGS and In_2S_3 layers.

The solar cells buffered with In_2S_3 layer deposited at three different flash rates were characterized by measuring their J - V characteristics. The PV parameters of the best flash- In_2S_3 and CdS reference devices are plotted in Fig. 12. The cells with In_2S_3 buffer layers yielded low efficiency compared to CdS reference cell primarily due to substantial loss in J_{sc} and fill factor (FF). The poor performance of In_2S_3 devices can be understood by presence of conduction band offset (cliff) at buffer/CIGS heterointerface as suggested by

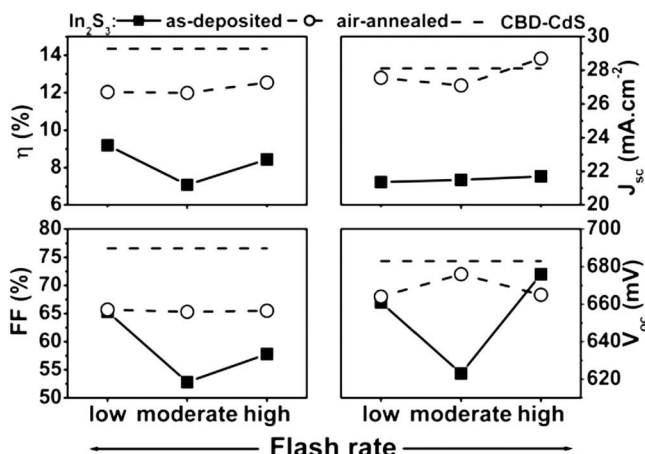


FIG. 12. PV parameters of the best CdS reference and flash- In_2S_3 buffered solar cells before and after air annealing for 20 min at 200°C (line connecting the data points serves as an eye-guide).

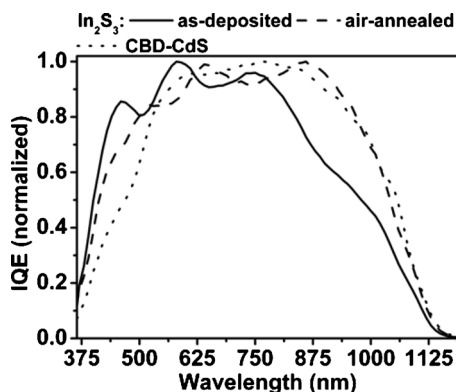


FIG. 13. IQE of CdS reference and high flash rate In_2S_3 buffered solar cells.

Jacob *et al.*⁴⁴ and other researchers^{4,45} in case of PVD- In_2S_3 /CIGS devices. The low temperature J - V measurement was performed to identify the dominant recombination path in the device with In_2S_3 buffer layer grown at high flash rate. The activation energy of 0.99 eV of the dominant recombination process, lower than the band gap (1.14 eV) of absorber, revealed the buffer/absorber heterointerface as the dominant recombination path in the device with In_2S_3 buffer layer. This finding indicated the possible existence of conduction band offset at buffer/CIGS heterointerface in flash- In_2S_3 device. Moreover, insufficient degree of surface inversion can further result in loss of cell performance.⁴⁶ The higher efficiency of the cell, due to high open-circuit voltage (V_{oc}) and FF, with low flash rate In_2S_3 buffer layer can be attributed to the superior quality of junction formed between CIGS absorber and chemically (near stoichiometry) and structurally (partially crystallized) less disordered In_2S_3 layer (Secs. III C and III D) leading to reduced interface recombination losses. Notably, except device with buffer grown at moderate flash rate, the open-circuit voltages of other devices were found to be close to V_{oc} of CdS device. The substitution of sulfur by oxygen in In_2S_3 causes reduction in electron affinity^{32,33} which leads to decrease in conduction band offset consequently, increasing V_{oc} and FF.^{45,47} In the present case of flash evaporated In_2S_3 buffer layer, an increase in oxygen content with increase in flash rate was determined by XPS investigation, thereby explaining the increase in V_{oc} and FF with rise in flash rate from moderate to high. The combined effect of reduction in conduction band offset due to presence of oxygen in In_2S_3 buffer layer and probable CIGS surface type-inversion induced by Cu migration from CIGS surface to In_2S_3 layer explains the increase in FF and J_{sc} as a result of air annealing of the complete device.

An insight into IQE of In_2S_3 device indicates the occurrence of type-inversion at CIGS surface as a consequence of air annealing. Figure 13 shows the IQE of (not the best but a randomly selected) device with In_2S_3 buffer layer grown at high flash rate and compares with CdS reference device. Owing to larger band gap of In_2S_3 layer than CdS, the enhanced carrier generation in blue region was observed in In_2S_3 device. The air annealing of the In_2S_3 buffered cell resulted in decrease in carrier collection efficiency in blue region followed by a remarkable improvement in long wavelength re-

sponse (480–1100 nm). The thermally induced elemental interdiffusion across In_2S_3 /CIGS heterointerface has been reported in literature.^{2,48} The experimental observations are in agreement with the formation of Cu depleted CIGS surface due to Cu diffusion from CIGS to In_2S_3 junction partner.^{49,50} The element Cu can readily diffuse from CIGS into In_2S_3 buffer layer altering its optical properties and the junction characteristics due to formation of graded interface with CIGS layer. The inclusion of Cu in In_2S_3 buffer layer lowers the band gap of the layer mainly affecting the valance band maximum position^{49,51} and thus the conduction band offset remains unaffected. Therefore, a decrease in carrier collection in blue region accompanied by a large enhancement for photons of $\lambda > 480$ nm can be understood by thermally assisted Cu diffusion from CIGS to In_2S_3 layer which has twofold effects, (a) lowering of band gap as a consequence of incorporation of Cu in structurally and chemically defective In_2S_3 layer and (b) the Cu depletion from CIGS surface which tends to form n-type (type-inversion) ordered vacancy compound resulting in inversion of the CIGS surface into n-type. Above discussion suggests that the diffusion of Cu from CIGS to In_2S_3 gives rise to enhanced collection efficiency in photon energy region below band gap of buffer layer which results in improved long wavelength response of the device as indicated in Fig. 13.

The out-diffusion of oxygen from i -ZnO to In_2S_3 even at room temperature deposition condition has been reported by Spiering *et al.*⁴⁸ In the present case of flash evaporated In_2S_3 , the layers are inherently contaminated with oxygen impurity with chemical disorder proportional to flash rate. This indicates that besides oxygen inclusion from growth process, its incorporation into In_2S_3 defect structure may further be favored by the presence of i -ZnO layer on top of In_2S_3 layer in the solar cell. Interestingly, the XPS analysis revealed that the solubility limit of oxygen in In_2S_3 resulting from air annealing was nearly same and thus is independent of flash rate (Fig. 10). This important finding can further be extended asserting that irrespective of different flash rates, the air annealing of flash- In_2S_3 buffered devices may cause same degree of reduction in conduction band offset at the In_2S_3 /CIGS heterointerface. This may explain the similar values of FF and V_{oc} obtained after air annealing of the device (Fig. 12). Hence, two concomitant effects of (a) oxygen incorporation during layer growth as well as from i -ZnO to In_2S_3 and (b) Cu diffusion from CIGS to In_2S_3 are responsible for enhanced PV performance after air annealing of the complete device.

It should be noted that as a consequence of air annealing of the device, the gain in photocurrent collection in long wavelength region ($480 < \lambda < 1190$ nm) is larger than the loss in blue region ($\lambda < 480$ nm). Moreover, the carrier collection efficiency of air-annealed In_2S_3 device in long wavelength region is similar to that of CdS device (Fig. 13). This implies that performance of In_2S_3 buffered device is strongly governed by degree of type-inversion of CIGS surface affecting the recombination losses occurring at the buffer/absorber interface.

Pursuing above discussion of carrier collection profile of the In_2S_3 /CIGS solar cell, the numerical calculation to quan-

tify the gain (or loss) in J_{sc} further confirmed the significant improvement in electronic quality of junction after air annealing treatment. The contribution from altered optical absorption (or reflection) from device originating from change in refractive indices of layers due to air annealing was found to be comparatively small. The total J_{sc} in the wavelength region λ_a and λ_b is defined as,

$$J_{sc} = \int_{\lambda_a}^{\lambda_b} q \times \Phi(\lambda) \times \text{EQE}(\lambda) \times d\lambda, \quad (7)$$

where $\Phi(\lambda)$ is incident photon flux density corresponding to standard AM 1.5 spectrum and “ q ” is elementary charge. The change in J_{sc} (ΔJ_{sc}^{1-2}) as a consequence of air annealing can be decoupled into optical (ΔJ_{sc}^{opt}), electronic (ΔJ_{sc}^{elc}), and other (ΔJ_{sc}^{oth}) components. The optical component, ΔJ_{sc}^{opt} , accounts for the change in optical absorption (or reflection) of the device caused by air annealing and can be expressed as,

$$\Delta J_{sc}^{opt} = \int_{\lambda_{ZnO}}^{\lambda_{CIGS}} q \times \Phi(\lambda) \times [A^2(\lambda) - A^1(\lambda)] \times d\lambda, \quad (8)$$

where, superscripts “1” and “2” notify as-deposited and air-annealed devices, respectively. $A(\lambda) [= 1 - R(\lambda)]$ is spectral absorption and $R(\lambda)$ spectral reflection of the device. The integral limits $\lambda_{CIGS} (= hc/E_g^{CIGS})$ and $\lambda_{ZnO} (= hc/E_g^{ZnO})$, where, “ h ” is Planck’s constant, “ c ” the speed of light and E_g^{ZnO} and E_g^{CIGS} are the band gap energies of ZnO and CIGS layers, respectively, define the usable photon energy region by the solar cell. IQE accounts for collection of charge carriers generated due to absorption of photons. The Eq. (9) denotes the electronic component of change in J_{sc} ,

$$\Delta J_{sc}^{elc} = \int_{\lambda_{ZnO}}^{\lambda_{CIGS}} q \times \Phi(\lambda) \times [\text{IQE}^2(\lambda) - \text{IQE}^1(\lambda)] \times d\lambda. \quad (9)$$

From above mathematical analysis, the optical and electric components of ΔJ_{sc}^{1-2} were calculated to be -0.48 mA.cm^{-2} and 4.1 mA.cm^{-2} , respectively. The negative sign of optical component, ΔJ_{sc}^{opt} , termed as “optical loss” indicated the current loss due to air annealing. On the other hand, the air annealing of the device led to a significant increase in J_{sc} referred as “electronic gain,” ΔJ_{sc}^{elc} . An absolute increase in short-circuit current of $\sim 7 \text{ mA.cm}^{-2}$ was measured from J - V measurement of the same device. This suggests that $\sim 58\%$ of the ΔJ_{sc}^{1-2} is originated from electronic component of J_{sc} indicating a significant improvement in the electronic quality of the junction and hence improving the carrier collection in the device.

IV. CONCLUSION

The application of TL model dielectric function ensured the reliability of determination of the optical constants of In_2S_3 layers deposited at three different flash rates. The optical band gap of the as-deposited layers was found to be a weak function of flash rate and increased after air annealing of the layers. With smooth and uniform growth, the layers were found to be inherently contaminated with oxygen impurity. The as-deposited layers were found to crystallize in

$\beta\text{-In}_2\text{S}_3$ phase. The chemical investigation confirmed the formation of nonstoichiometric layer with respect to sulfur content with degree of nonstoichiometry proportional to flash rate. The morphological, optical, structural, and chemical studies of flash evaporated buffer layers indicated the formation of structurally and chemically disordered layer with increase in degree of disorder with rise in flash rate. A layer growth model supporting growth and properties of layer has been proposed.

With minor impact on the optical reflection losses from flash- In_2S_3 buffered solar cell, the air annealing of the complete device resulted in marked improvement in the electronic quality of the cell leading to a significant gain in short-circuit current. The combined positive effects of oxygen incorporation in In_2S_3 and CIGS surface type-inversion as a result of air annealing was analytically found to be primarily responsible for enhancement in the PV performance of the solar cell.

ACKNOWLEDGMENTS

The financial support from Swiss National Science Foundation and Swiss Federal Office of Energy is gratefully acknowledged.

- ¹A. R. Barron, *Adv. Mater. Opt. Electron.* **5**, 245 (1995).
- ²N. Naghavi, S. Spiering, M. Powalla, B. Cavana, and D. Lincot, *Prog. Photovoltaics* **11**, 437 (2003).
- ³D. Hariskos, M. Ruckh, U. Rühle, T. Walter, H. W. Schock, J. Hedström, and L. Stolt, *Sol. Energy Mater. Sol. Cells* **41–42**, 345 (1996).
- ⁴A. Strohm, L. Eisenmann, R. K. Gebhardt, A. Harding, T. Schlötzer, D. Abou-Ras, and H. W. Schock, *Thin Solid Films* **480–481**, 162 (2005).
- ⁵R. H. Bube and W. H. McCarroll, *J. Phys. Chem. Solids* **10**, 333 (1959).
- ⁶W.-T. Kim and C.-D. Kim, *J. Appl. Phys.* **60**, 2631 (1986).
- ⁷J. Herrero and J. Ortega, *Sol. Energy Mater.* **17**, 357 (1988).
- ⁸J. George, K. S. Joseph, B. Pradeep, and T. I. Palson, *Phys. Status Solidi A* **106**, 123 (1988).
- ⁹T. Asikainen, M. Ritala, and M. Leskelä, *Appl. Surf. Sci.* **82–83**, 122 (1994).
- ¹⁰Y. Yasaki, N. Sonoyama, and T. Sakata, *J. Electroanal. Chem.* **469**, 116 (1999).
- ¹¹N. Barreau, S. Marsillac, D. Albertini, and J. C. Bernède, *Thin Solid Films* **403–404**, 331 (2002).
- ¹²D. Hariskos, R. Menner, S. Spiering, A. Eicke, M. Powalla, K. Ellmer, M. Oertel, and B. Dimmler, Proceedings of the 19th European Photovoltaic Solar Energy Conference and Exhibition, 7–11 June 2004, Paris, France, p. 1894.
- ¹³N. Naghavi, R. Henriquez, V. Laptev, and D. Lincot, *Appl. Surf. Sci.* **222**, 65 (2004).
- ¹⁴J. Sterner, J. Malmström, and L. Stolt, *Prog. Photovoltaics* **13**, 179 (2005).
- ¹⁵R. Robles, N. Barreau, A. Vega, S. Marsillac, J. C. Bernède, and A. Mokrani, *Opt. Mater. (Amsterdam, Neth.)* **27**, 647 (2005).
- ¹⁶N. A. Allsop, A. Schönmann, A. Belaidi, H.-J. Muffler, B. Mertesacker, W. Bohne, E. Strub, J. Röhrich, M. C. Lux-Steiner, and C.-H. Fisher, *Thin Solid Films* **513**, 52 (2006).
- ¹⁷R. Verma, S. Buecheler, D. Corica, A. Chirila, S. Seyrling, J. Perrenoud, D. Guettler, C. J. Hibberd, and A. N. Tiwari, Proceedings of the 23rd European Photovoltaic Solar Energy Conference and Exhibition, 1–5 September 2008, Valencia, Spain, p. 2179.
- ¹⁸P. Pistor, R. Caballero, D. Hariskos, V. Izquierdo-Roca, R. Wächter, S. Schorr, and R. Klenk, *Sol. Energy Mater. Sol. Cells*, **93**, 148 (2009).
- ¹⁹R. D. L. Kristensen, S. N. Sahu, and D. Haneman, *Sol. Energy Mater.* **17**, 329 (1988).
- ²⁰A. Chirila, D. Guettler, D. Brémaud, S. Buecheler, R. Verma, S. Seyrling, S. Nishiwaki, S. Haenni, G. Bilger, and A. N. Tiwari, Proceedings of the 34th IEEE Photovoltaic Specialist Conference, Philadelphia, USA, 7–12 June 2009, p. 000812.
- ²¹K. Vedam, *Thin Solid Films* **313–314**, 1 (1998).
- ²²K. Orgassa, U. Rau, Q. N. Nguyen, H. W. Schock, and J. H. Werner, *Prog.*

- Photovoltaics* **10**, 457 (2002).
- ²³J. F. Trigo, B. Asenjo, J. Herrero, and M. T. Gutierrez, *Sol. Energy Mater. Sol. Cells* **92**, 1145 (2008).
 - ²⁴M. M. El-Nahass, B. A. Khalifa, H. S. Soliman, and M. A. M. Seyam, *Thin Solid Films* **515**, 1796 (2006).
 - ²⁵N. Kamoun, R. Bennaceur, M. Amlouk, S. Belgacem, N. Mliki, J. M. Frigerio, and M. L. Theye, *Phys. Status Solidi A*, **169**, 97 (1998).
 - ²⁶S. Marsillac, N. Barreau, H. Khatri, J. Li, D. Sainju, A. Parikh, N. J. Podraze, and R. W. Collins, *Phys. Status Solidi C* **5**, 1244 (2008).
 - ²⁷D. Datta and S. Kumar, *J. Appl. Phys.* **106**, 074517 (2009).
 - ²⁸N. Laidani, R. Bartali, G. Gottardi, M. Anderle, and P. Cheyssac, *J. Phys.: Condens. Matter* **20**, 015216 (2008).
 - ²⁹G. E. Jellison, Jr. and F. A. Modine, *Appl. Phys. Lett.* **69**, 371 (1996).
 - ³⁰D. Datta and S. Kumar, *Sol. Energy Mater. Sol. Cells* **94**, 420 (2010).
 - ³¹J. D. Dow and D. Redfield, *Phys. Rev. B* **5**, 594 (1972).
 - ³²N. Barreau, J. C. Bernède, S. Marsillac, and A. Mokrani, *J. Cryst. Growth* **235**, 439 (2002).
 - ³³N. Barreau, S. Marsillac, J. C. Bernède, and L. Assmann, *J. Appl. Phys.* **93**, 5456 (2003).
 - ³⁴N. Barreau, J. C. Bernède, C. Deudon, L. Brohan, and S. Marsillac, *J. Cryst. Growth* **241**, 4 (2002).
 - ³⁵N. Barreau, J. C. Bernède, and S. Marsillac, *J. Cryst. Growth* **241**, 51 (2002).
 - ³⁶S. Aljishi, J. D. Cohen, S. Jin, and L. Ley, *Phys. Rev. Lett.* **64**, 2811 (1990).
 - ³⁷R. Jayakrishnan, T. T. John, C. S. Kartha, K. P. Vijayakumar, T. Abe, and Y. Kashiwaba, *Semicond. Sci. Technol.* **20**, 1162 (2005).
 - ³⁸A. R. Miller and A. W. Searcy, *J. Phys. Chem.* **67**, 2400 (1963).
 - ³⁹A. R. Miller and A. W. Seracy, *J. Phys. Chem.* **69**, 3826 (1965).
 - ⁴⁰R. Colin and J. Drowart, *Trans. Faraday Soc.* **64**, 2611 (1968).
 - ⁴¹H. L. Hwang, C. C. Tu, J. S. Maa, and C. Y. Sun, *Sol. Energy Mater.* **2**, 433 (1980).
 - ⁴²N. Barreau, C. Deudon, A. Lafond, S. Gall, and J. Kessler, *Sol. Energy Mater. Sol. Cells* **90**, 1840 (2006).
 - ⁴³F. Py, M. Womes, J. M. Durand, J. Olivier-Fourcade, J. C. Jumas, J. M. Esteve, and R. C. Karnatak, *J. Alloys Compd.* **178**, 297 (1992).
 - ⁴⁴F. Jacob, N. Barreau, S. Gall, and J. Kessler, *Thin Solid Films* **515**, 6028 (2007).
 - ⁴⁵S. Gall, N. Barreau, F. Jacob, S. Harel, and J. Kessler, *Thin Solid Films* **515**, 6076 (2007).
 - ⁴⁶R. Klenk, *Thin Solid Films* **387**, 135 (2001).
 - ⁴⁷T. Minemoto, Y. Hashimoto, W. Shams-Kolahi, T. Satoh, T. Negami, H. Takakura, and Y. Hamakawa, *Sol. Energy Mater. Sol. Cells* **75**, 121 (2003).
 - ⁴⁸S. Spiering, A. Eicke, D. Hariskos, M. Powalla, N. Naghavi, and D. Lin-cot, *Thin Solid Films* **451–452**, 562 (2004).
 - ⁴⁹N. Barreau, S. Gall, S. Marsillac, J. Kessler, and A. Rockett, Proceedings of the 20th European Photovoltaic Solar Energy Conference and Exhibition, 6–10 June 2005, Barcelona, Spain, p. 1717.
 - ⁵⁰D. Abou-Ras, D. Rudmann, G. Kostorz, S. Spiering, M. Powalla, and A. N. Tiwari, *J. Appl. Phys.* **97**, 084908 (2005).
 - ⁵¹N. Barreau, J. C. Bernède, and J. Kessler, Proceedings of the 19th European Photovoltaic Solar Energy Conference and Exhibition, 7–11 June 2004, Paris, France, p. 223.